Chapter 3 – Temperature- and Pressure-Dependent Branching Ratios of the OH + NO_2 Reaction Using Cavity Ringdown Spectroscopy

3.1 – Abstract

The reaction between OH and NO_2 has long been known to play an important role in ozone production over urban areas, due to its ability to sequester NO_x as nitric acid ($HONO_2$). However, a minor channel leading to peroxynitrous acid (HOONO) formation can also occur. Due to the instability of this molecule, it is believed to quickly redissociate back to OH and NO_2, thereby decreasing this reaction's efficiency as a sink for nitrogen oxides (NO_x). The branching ratio between these channels, denoted α = [HOONO]/ [$HONO_2$], varies as a function of temperature and pressure, but experimental measurements of these values are limited. Here, we present measurements of the temperature- and pressure-dependence of the branching ratio of this reaction over a range of temperatures (255 – 333 K) and pressures (50 – 700 torr). Reactions were initiated by pulsed laser photolysis in a flow reactor, and HOONO and $HONO_2$ formed in real time were detected by mid-infrared cavity ringdown spectroscopy. By combining our results with the latest recommendations of the total OH + NO_2 rate constant from the JPL data evaluation, we provide individual rate constants for the formation of HOONO and of $HONO_2$.

3.2 – Introduction

Throughout the troposphere and stratosphere, the coupling of the HO_x (HO_x = OH and HO_2) and NO_x (NO_x = NO and NO_2) families plays an important role in a region's air quality. OH radicals are the primary source that oxidize stable, long-lived molecules in the atmosphere, while NO_2 radicals lead to the formation of photochemical smog in urban environments.[1] The most important coupling between the HO_x and NO_x families is the termolecular radical-terminating reaction between OH and NO_2.

$$OH + NO_2 + M \rightarrow HONO_2 + M \quad \text{(R3.1a)}$$

$$OH + NO_2 + M \rightarrow HOONO + M \quad \text{(R3.1b)}$$

The nitric acid, $HONO_2$, formed from R3.1a is long-lived in the atmosphere, thus serving as a sink for both HO_x and NO_x. This reaction plays an important role in atmospheric modelling by sequestering radical concentrations; a sensitivity analysis studying the impact of over 900 model inputs on the modelled ozone concentration in urban environments found that the total rate constant $k_{3.1}$ ($k_{3.1} = k_{3.1a} + k_{3.1b}$) was the most important rate constant, and second-most important parameter overall.[2] Under urban conditions (low VOCs, high NO_x), R3.1a is responsible for a paradoxical decrease in ozone production with increasing NO_x, by removing OH and inhibiting OH-initiated oxidation of VOCs.

The alternate pathway, shown in R3.1b, leads to the formation of peroxynitrous acid, HOONO, was first proposed in 1983 by Robertshaw and Smith.[3] HOONO was not observed until 2002, when the HOONO arising from R3.1b was detected through vibrational overtone photodissociation spectroscopy.[4] Since then, it has been the subject of several experimental studies[4-8] in order to better understand the molecule. HOONO quickly decomposes to regenerate OH and NO_2 at room temperature and consequently reduces

efficiency of R3.1 as a sink.[9] The potential energy surface of the reaction can be seen in Figure 3.1. These results indicate that there are two conformers of HOONO that can be formed, known as *cis-cis* and *trans-perp*, with the *cis-cis* being the lower energy of the two, as seen in Figure 3.1. Under atmospheric conditions, the *trans-perp* HOONO isomerizes to *cis-cis*, which is stabilized by an internal hydrogen bond between the hydrogen and terminal oxygen.[7]

While there have been a number of experimental studies measuring $k_{3.1}$ at a wide range of temperatures and pressures by monitoring the decay of OH in an excess of NO_2, as summarized and evaluated by JPL[9] and IUPAC,[10] experimental measurements of the branching ratio of the products, $\alpha = k_{3.1b}/k_{3.1a}$ (= [HOONO]/[$HONO_2$]), are scarce. Furthermore, α changes as a function of both temperature and pressure, making it necessary to measure over a wide range of conditions. The only two direct measurements of the branching ratio are from Mollner et al.,[11] who measured it between 50 and 750 torr at room temperature, and Bean et al.,[6] who studied it at 20 torr from 270 to 360 K; both studies used pulsed laser photolysis in conjunction with mid-IR spectroscopy to measure the ν_1 bands of HOONO and $HONO_2$. Hippler et al.[12-13] extracted rate constants for the two channels from their high pressure measurements and fall-off curve analysis of the OH decay. Troe[14] re-analyzed the data of Mollner et al. and Hippler et al. in order to separately determine the rate constants $k_{3.1a}$ and $k_{3.1b}$.

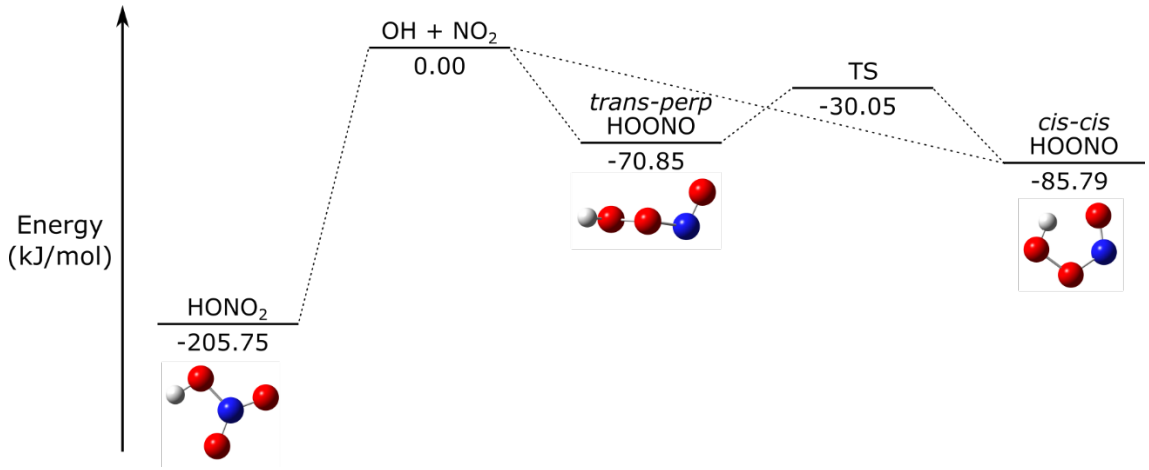

Figure 3.1: Simplified potential energy surface of the OH + NO_2 reaction in kJ/mol; molecular geometries are from the Active Thermochemical Tables[15] and the transition state energy is the experimental value of Fry et al.[7]

Current recommendations for the branching ratio (and thus, $k_{3.1a}$ and $k_{3.1b}$) from the JPL data evaluation are based on the RRKM (Rice–Ramsperger–Kassel–Marcus) master equation calculations performed by Golden et al.,[16] while IUPAC's evaluation is based on the results of Mollner et al. and Troe. The uncertainties present in the determined parameters are large: JPL recommends an uncertainty factor 1.3 for $k_{3.1a}$ and 1.5 for $k_{3.1b}$ at 298 K, with increasing uncertainty at other temperatures. IUPAC recommends uncertainty factors of 1.12 and 2.0 for the low and high-pressure limits of $k_{3.1a}$, respectively, and 1.26 and 2.0 for the low and high-pressure limits of $k_{3.1b}$ at 300 K. As the temperature moves away from 298 K, these uncertainties will further increase. These large uncertainties propagate into the atmospheric models that are reliant on these evaluations. A recent modeling analysis studied the impact of these uncertainties on four key metrics from the GEOS-Chem chemical transport model: annual tropospheric ozone burden, surface ozone concentration, tropospheric OH concentration and tropospheric methane lifetime.[17] Their results found that R3.1a was the single largest source of uncertainty among inorganic rate constants and photolysis rates across all metrics, and recommend focusing efforts on

improving this rate constant among others to improve our knowledge of atmospheric composition.

Due to both the high uncertainty of these rate constants in current recommendations and the importance of this reaction for atmospheric modelling, we have extended the work of Mollner et al. and Bean et al. In this study, we have measured the pressure-dependent branching ratio α over a wide range of temperatures, from 255 to 333 K, and pressures 50 to 700 torr. By combining these measurements with previous measurements of $k_{3.1}$, we have also determined $k_{3.1a}$ and $k_{3.1b}$.

3.3 – Experimental Methods

These experiments used a pulsed laser photolysis-cavity ringdown spectroscopy (PLP-CRDS) apparatus, which has been described previously in the literature[11, 18-19] and in Chapter 2. Briefly, reactions are initiated in a temperature-controlled flow cell, described in Chapter 2, by pulsed UV light at 248 nm to generate OH in the presence of NO_2. The ν_1 OH-stretch bands of the primary $HONO_2$ and HOONO products were detected at a fixed delay time after the completion of the reaction, by pulsed mid-infrared cavity ringdown spectroscopy. Concentrations were determined by integrating the absorption bands, using computed absorption band intensities.

The 532 nm light pulses from a frequency-doubled Nd:YAG laser, operated at 10 Hz, passed through a 70/30 beamsplitter, where 30% of the 532 nm light pumped a tuneable dye laser containing DCM dye. The output of the dye laser was recombined with the remaining (70% transmitted) 532 nm light and sent into nonlinear KDP crystals, which produced mid-IR light as the idler by difference frequency generation. The mid-IR light was filtered to remove pump and signal radiation and then coupled into an optical cavity

formed by two highly reflective mirrors (R > 0.9998, CRD Optics) enclosing the reaction volume in the flow cell. The output was detected by a liquid nitrogen cooled InSb detector. This instrument operates in the 3200 – 3750 cm^{-1} range, limited by the mirror reflectivity, which allowed us to detect the ν_1 OH stretches of HOONO and $HONO_2$, as has been previously observed with this instrument in our group.[6, 11] UV pulses at 248 nm were generated by an excimer laser (Lambda Physik 210i) and focused into the reaction cell perpendicularly to the IR cavity axis to generate OH radicals. Experiments were performed at 10 Hz. The total gas flow rate was sufficient to ensure complete exchange of gas in the flow reactor between pulses.

Sixteen ringdowns decay traces were recorded and averaged at each frequency; each were taken with and without the excimer firing at each point in our spectrum (referred to subsequently as the 'excimer-on' and 'excimer-off' spectra, respectively). A mirror curve, taken under vacuum at each temperature studied, was recorded daily, and fit to determine the reflectivity of the mirrors as a function of frequency.

3.3.1 – Radical Chemistry

OH was generated via the photolysis of O_3 at 248 nm, followed by subsequent reaction with H_2:

$$O_3 + h\nu \rightarrow O(^1D) + O_2 \quad \text{(R3.2)}$$

$$O(^1D) + H_2 \rightarrow OH + H \quad \text{(R3.3)}$$

NO_2 was added in excess, such that the OH + NO_2 reaction is under pseudo-first order conditions; typical gas concentrations were $[O_3] = 1 - 15 \times 10^{15}$ cm^{-3}, $[NO_2] = 1 - 10 \times 10^{15}$ cm^{-3}, and $[H_2] = 5 - 25 \times 10^{17}$ cm^{-3}, with the balance N_2. H_2 concentrations were increased at higher pressures to minimize quenching of the $O(^1D)$ by N_2. Ozone was generated from

flowing O_2 through a corona discharge ozonizer. To minimize secondary chemistry, the ozone was purified to remove O_2, by condensing the ozone on silica gel in a metal trap cooled by a dry ice/acetone bath. The O_2 was removed by vacuum. During the experiment, the ozone was introduced into the flow cell by flowing N_2 through the trapped ozone. Before mixing with other gases, the O_3 concentration was measured by flowing the O_3/N_2 mixture through a 1 m long flow cell. UV light at 307.6 nm ($\sigma_{307.6} = 1.4 \times 10^{-19}$ cm^2)[9] from a Zn lamp was passed through the cell and was detected with a monochromator and photomultiplier tube. The ozone concentration was recorded at the beginning and end of each scan to observe any fluctuations in O_3 concentration; typical O_3 concentrations were stable to within 15%. Measurements with larger fluctuations in [O_3] were excluded from fits.

The hydrogen atoms formed as a by-product of R3.3 can undergo two fates: reaction with NO_2 or with O_3.

$$H + NO_2 \rightarrow OH + NO \quad \text{(R3.4)}$$

$$H + O_3 \rightarrow OH + O_2 \quad \text{(R3.5)}$$

These additional OH radicals from both channels undergo further reaction with NO_2. The presence of NO and O_2 from this chemistry may lead to side chemistry that interferes with our spectroscopic measurements, as the reactions with NO lead to the production of HONO from

$$OH + NO + M \rightarrow HONO + M \quad \text{(R3.6)}$$

While O_2 could lead to HO_2 formation

$$H + O_2 + M \rightarrow HO_2 + M \quad \text{(R3.7)}$$

Spectral features arising from small concentrations of HONO were observed and therefore were included in our spectral fitting program. HO_2 and its likely end product, HO_2NO_2, were not observed and were therefore omitted.

OH produced from R3.3 is known to be vibrationally excited, resulting in up to OH (v = 4).[20] Mollner et al., who also used R3.3 to produce OH, performed several experiments to verify whether this affected the measured branching ratio, by using an alternate source of OH, $O(^1D) + CH_4$, which produces a much smaller quantity of excited OH radicals.[21] They did not find any change in their measured values from these experiments, suggesting that the presence of hot OH does not affect the branching ratios. While vibrational relaxation rates for OH (v = 1 – 4) with the gases present in our system have not been measured, Smith and Williams previously measured the rate constant for OH (v = 1) relaxation by NO_2 at room temperature to be 4.8×10^{-11} cm^3 s^{-1}.[22] Assuming that higher vibrational states of OH relax at the same rate, a kinetic model indicates that all OH is vibrationally cooled within 10 – 100 μs under our NO_2 concentrations. This is likely an overestimate of the lifetime of vibrationally-excited OH within our system, as higher vibrational levels are likely to have larger rate constants for vibrational relaxation. Together, these results suggest that influence of vibrationally-excited OH on our branching ratio measurements is negligible.

Spectra were measured 500 μs after photolysis. As can be seen in Figure 3.2, time-dependent measurements of HOONO and $HONO_2$ indicated that this reaction is complete in roughly 150 μs; the signal remains stable for up to 3 ms in our system before being vacuumed out, even at our highest temperatures of 333 K. The time-dependent

measurements agree well with a simple model of the product appearance based on $k_{3.1}$, the experimental conditions and NO_2 concentration used in experiments (4.4×10^{15} cm^{-3}).

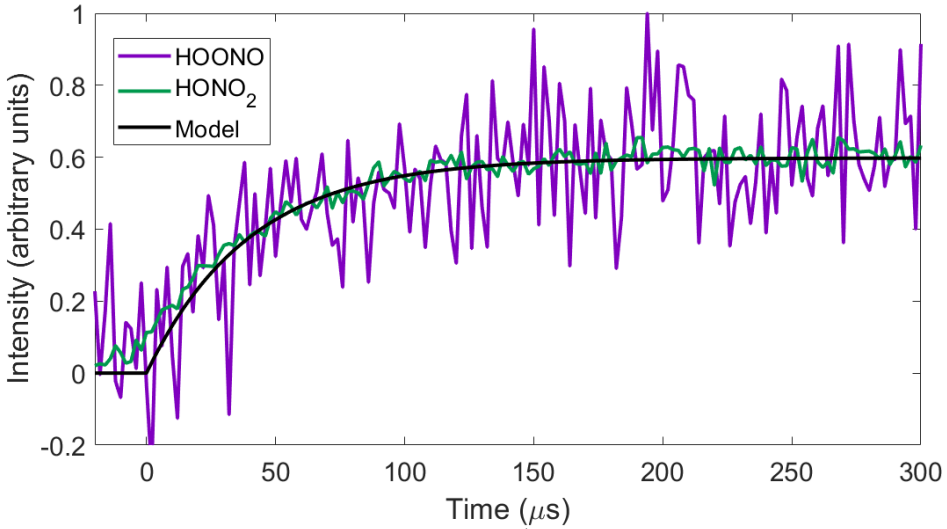

Figure 3.2: Time traces of HOONO at 3307 cm^{-1} (purple) and $HONO_2$ at 3520 cm^{-1} (green) at 333 K and 300 torr showing the formation of products; the excimer fires at 0 μs to initiate radical chemistry. The modelled appearance of products, based on the experimental conditions and NO_2 concentrations used is shown in black.

3.3.2 – Spectroscopy and Spectral Fitting

A typical experimental spectrum, measured from 3250 – 3630 cm^{-1} with a step size of 2 cm^{-1}, is shown in Figure 3.3. This step size was used because it provided sufficient resolution to clearly identify the key spectral features, while allowing us to minimize uncertainties from fluctuations in ozone concentration during a scan. Typical scan times were 25 minutes to record a full spectrum. The ν_1 band of $HONO_2$, centered at 3550 cm^{-1}, was the dominant feature, while its $2\nu_2$ band can be seen in the inset at 3400 cm^{-1}. The *cis-cis* conformer of HOONO was observed at 3306 cm^{-1}. Weak features of both c*is*-HONO and *trans*-HONO arising from secondary chemistry could be also be observed in some spectra, most notably the Q-branch of the ν_1 OH stretch of *trans*-HONO at 3590 cm^{-1}.

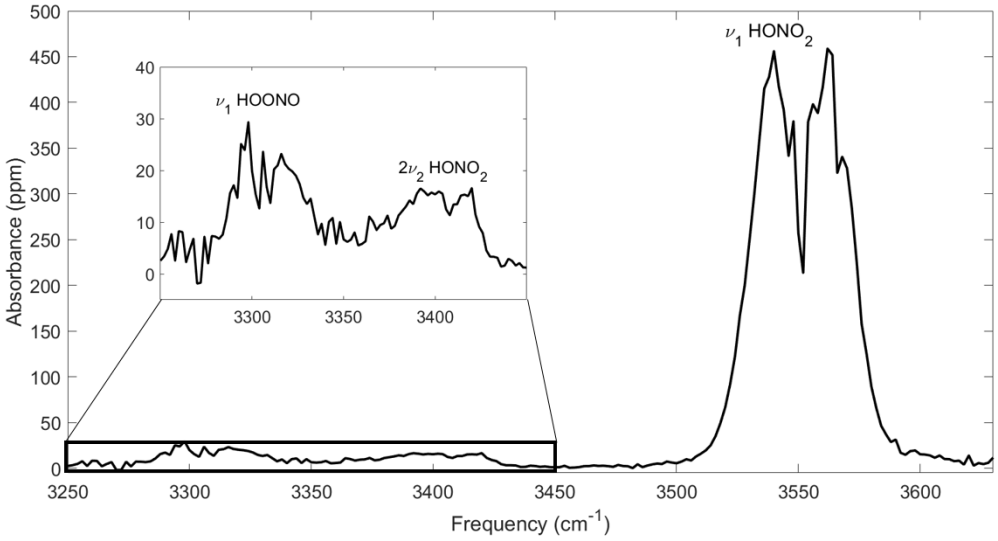

Figure 3.3: Experimental spectrum taken at 283 K and 500 torr, 500 μs after photolysis, showing the ν_1 bands of HOONO and $HONO_2$ and the $2\nu_2$ band of $HONO_2$. This spectrum is obtained by subtracting the excimer-off spectrum from the corresponding excimer-on spectrum.

Each spectrum was fit using a nonlinear least squares fit in Matlab to a sum of reference spectra. The reference spectra were either from the PNNL spectral database[23] or, for HOONO, measured in our lab.[6] The PNNL spectral database shows that $HONO_2$, N_2O_4 and HONO spectra do not change with temperature. Any change in the spectrum of HOONO will be accounted for by $f_{Boltz}(T)$, as discussed below in Section 3.3.3. The total absorbances of HOONO and $HONO_2$ (A_{HOONO} and A_{HONO_2} respectively) was obtained by integrating the spectral features from our fits, as discussed below. The branching ratio $\alpha(T, p)$ was obtained:

$$\alpha = \frac{\int A_{HOONO}}{\int A_{HONO_2}} \frac{\sigma_{HONO_2}}{\sigma_{HOONO}} f_{Boltz}(T) \qquad \text{(Equation 4.1)}$$

The ratio of the cross sections ($\sigma_{HONO_2}/\sigma_{HOONO}$) has previously been calculated by Mollner et al.[11] using CCSD(T)/ANO to be 2.71, while $f_{Boltz}(T)$ is a temperature-

dependent correction factor for the impact of the stretch-torsion coupling of HOONO on our measurements of A_{HOONO}, as discussed in the following section.

3.3.3 – HOONO Spectroscopy

As discussed in Section 3.1, there are two stable conformers of HOONO, *trans-perp* HOONO and *cis-cis* HOONO; only the latter of which we observe in our spectrum due to the rapid isomerization of *trans-perp* HOONO.[7] The presence of the internal hydrogen bond between the terminal oxygen and the hydrogen in *cis-cis* HOONO redshifts its ν_1 OH stretch; previous mid-IR measurements found that this band is centered at 3306 cm^{-1}.[6] Based on these measurements, we have determined A_{HOONO} by fitting our experimental measurements of the *cis-cis* HOONO stretch region (3264 – 3352 cm^{-1}) to a room-temperature reference spectrum from Mollner et al.[11]

However, stretch-torsion coupling between the OH stretch and two low-lying torsional states must be corrected for in our analysis. These torsional modes, belonging to the ν_9 HOON (n = 1 mode centered at 312 cm^{-1}) and ν_8 OONO (n = 1 mode centered at 484 cm^{-1}) modes,[24] have significant populations at room temperature. These torsionally-excited states change the position of the HOONO ν_1 stretch; extensive calculations have been done by McCoy et al.[24] on this effect for up to n = 8 of ν_9 and n = 2 of ν_8, as well as combinations of these modes. These calculations indicate that the ν_1 band can shift out of our integration range in some of these torsionally excited states. In order to account for how this affects the determination of A_{HOONO}, we incorporated a correction factor, $f_{Boltz}(T)$, based on the Boltzmann distribution of torsionally excited states and whether the center frequency of the ν_1 state is inside the A_{HOONO} integration region. Further details of these calculations and $f_{Boltz}(T)$ can be found in Mollner et al.[11] and McCoy et al.[24]

A_{HOONO} was fit by subtracting the excimer-off spectrum from the excimer-on spectrum, which removes any background absorbance from non-photolytically generated molecules. Spectra were fit between 3250 and 3440 cm^{-1} to avoid ν_1 stretch of $HONO_2$, which is the most intense peak in our spectra. The intensities of the ν_1 stretch of HOONO and $2\nu_2$ stretch of $HONO_2$ were fit, along with background absorbance of HONO and a sloped baseline. The intensity of the ν_1 stretch of HOONO was subsequently integrated to determine A_{HOONO}.

3.3.4 – $HONO_2$ Spectroscopy

The ν_1 band of $HONO_2$ has been the subject of numerous studies. Chackerian et al. studied the integrated cross sections from 278 to 323 K and observed no change in the cross sections of this band.[25] Measurements taken at 255 and 333 K with our CRDS system also found no change in the spectral shape. Therefore, we assumed the shape of the ν_1 band of $HONO_2$ to be temperature-independent over the temperature range studied here. Spectra were fit to a reference from PNNL,[23] which was integrated between 3476 and 3630 cm^{-1} to determine A_{HONO_2}.

Our previous measurements of the ν_1 stretch of $HONO_2$ have found that a correction factor is necessary in order to accurately quantify [$HONO_2$].[11] This correction factor arises from an effect in cavity ringdown spectroscopy originally described by Yalin and Zare,[26] which occurs when the linewidth of the laser is larger than spectroscopic features being probed. This leads to multiexponential ringdowns that, when fit to a single exponential decay, provide a value that underestimates the true absorbance. This effect is dependent on the pressure of the system, and the intensity of the absorption features. As the most intense feature in our experimental spectrum, our quantification of [$HONO_2$] from its ν_1 stretch is

impacted and must be corrected for to obtain accurate branching ratios. We applied this correction to the most intense parts of our spectrum, 3524 - 3576 cm^{-1}. The correction factor, previously used in Mollner et al. and checked with extensive measurements of $HONO_2$ at varying pressures and concentrations,[11] convolves a high resolution spectrum of the $HONO_2$ ν_1 stretch with pressure broadening parameters and a 1 cm^{-1} bandwidth laser pulse to simulate the experimental ringdown decay and convert to A_{HONO_2}.

The ν_1 stretch of $HONO_2$ was observed in our excimer-off spectra, indicating that some level of $HONO_2$ was present in our system before photolysis occurs, most likely due to heterogeneous chemistry occurring within the gas lines. While not as intense as the excimer-on $HONO_2$, in order to accurately determine A_{HONO_2}, we separately analyzed the excimer-on and excimer-off spectra. The absorbance due to the reflectivity of the mirrors is removed from these spectra. The excimer-off spectra are fit with the ν_1 and $2\nu_2$ peaks of $HONO_2$ as well as an overtone of N_2O_4. For the excimer-on spectra, the spectra of HOONO and HONO are also included in the fit. Both spectra also include a sloped baseline, or when necessary due to differences between our mirror curve and experimental spectrum, a quadratic baseline. The correction factor for multiexponential ringdowns is applied to the ν_1 band of $HONO_2$, as discussed in Section 3.3.4. The intensity of both the excimer-on and excimer-off spectra are subsequently integrated and the difference is taken as our value of A_{HONO_2}.

Our fitting routine found that the intensity of the Q-branch of the ν_1 band of $HONO_2$, located at 3552 cm^{-1} is not consistent throughout our data or with the intensity predicted by our fitting routine, likely due the sharpness of the feature and small calibration offsets

in our frequency axis. This point is therefore excluded from our fit. We do not find any evidence of these frequency offsets affecting the rest of our experimental spectra.

3.4 – Results and Discussion

3.4.1 – Branching Ratio Measurements

Measurements were taken at nine temperatures between 255 and 333 K in roughly 10 K steps, with pressures varying from 50 to 700 torr at each temperature. For each temperature and pressure point, spectra were recorded multiple times (typically five). Each spectrum was fit with our reference spectra, as discussed above, to determine the final $HONO_2$ and HOONO concentrations, and the resulting branching ratio was determined from a weighted average.

As the reaction between OH and NO_2 is a termolecular reaction, we investigated whether the identity of the third body affected our results. H_2 was a present in excess in our experiments to form OH, and therefore we varied the ratio of H_2 in the total flow at 293 K and 100 torr to determine the effect of the bath gases on our branching ratio measurements. As can be seen in Figure 3.4, we do not observe a change in the branching ratio as a function of the bath gas ratio.

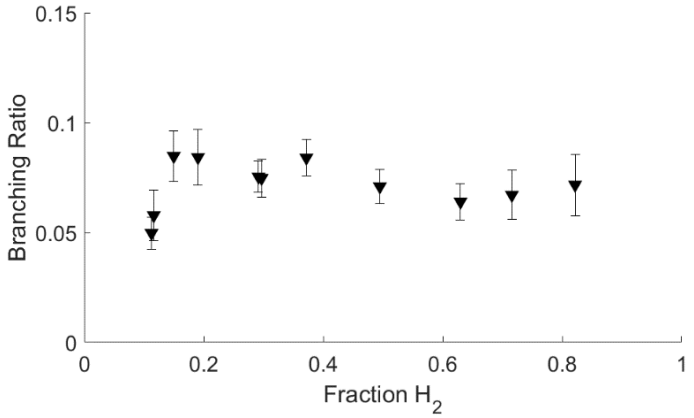

Figure 3.4. Experiments measuring the branching ratio as a function of H_2 fraction at 100 torr and 293 K, indicating that our measurements do not change as a function of H_2 concentration.

The weighted averages for the branching ratios can be seen in Table 3.1 A comparison between our measured branching ratios and those predicted by the JPL and IUPAC evaluations at 283 and 323 K can be seen in Figure 3.5. We find that at higher temperatures, the branching ratios from the data evaluations are close to our measurements, while at colder temperatures more relevant to the troposphere, the predictions overestimate α. This implies that either HOONO production is overestimated or $HONO_2$ production is underestimated in the current evaluations at these temperatures.

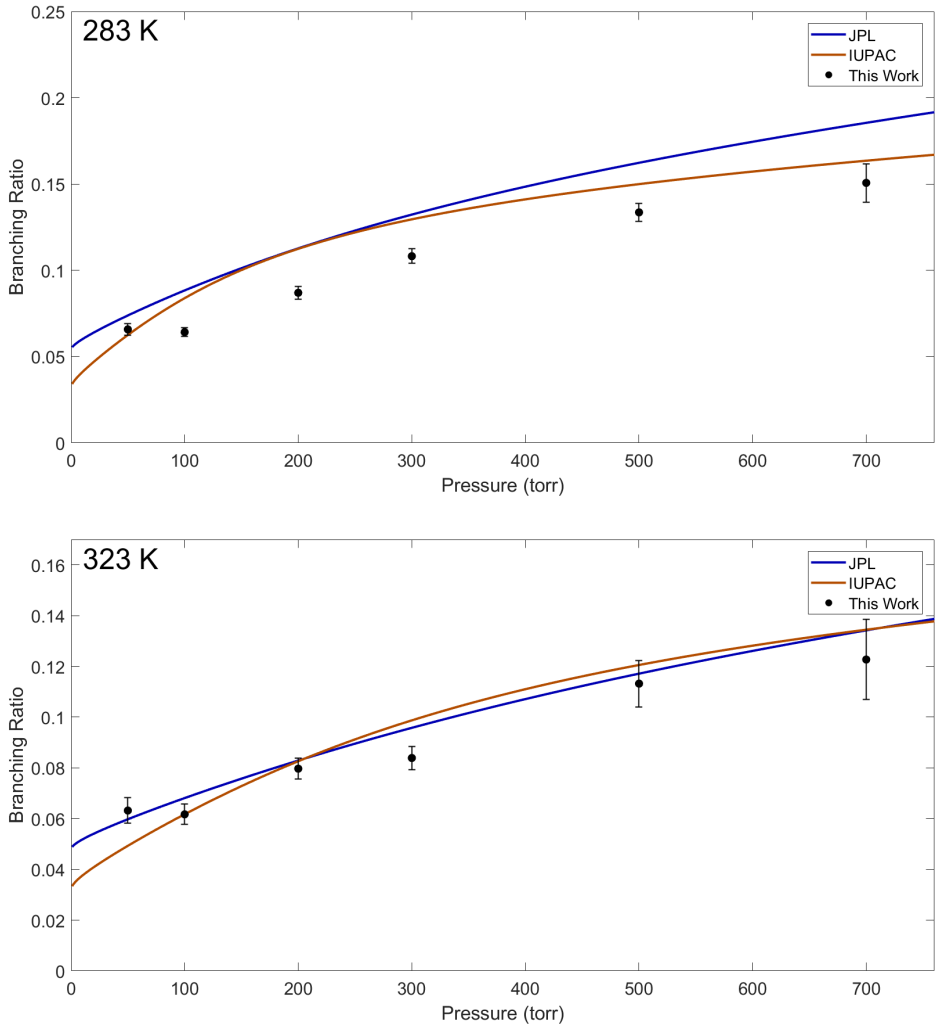

Figure 3.5: The branching ratios $k_{3.1b}/k_{3.1a}$ from the JPL and IUPAC data evaluations at 283 and 323 K, as compared to the experimental values measured in this work.

Table 3.1: The weighted averages of all branching ratios measured in this work.

Temp (K)	Pressure (torr)	Branching Ratio	Uncertainty	Number of Measurements
333	50	0.0749	0.0067	10
333	100	0.0625	0.0054	7
333	200	0.0819	0.0067	7
333	300	0.0831	0.0071	5
333	500	0.0958	0.0068	4
333	700	0.1214	0.0102	5
323	50	0.0632	0.0050	5
323	100	0.0617	0.0040	5
323	200	0.0797	0.0041	6
323	300	0.0839	0.0046	6
323	500	0.1132	0.0092	4
323	700	0.1227	0.0158	5
313	50	0.0459	0.0025	7
313	100	0.0549	0.0031	7
313	200	0.0687	0.0034	6
313	300	0.0847	0.0039	6
313	500	0.0858	0.0047	5
313	700	0.1164	0.0051	5
303	50	0.0564	0.0037	4
303	100	0.0657	0.0033	5
303	200	0.0834	0.0038	5
303	300	0.0882	0.0051	3
303	500	0.1060	0.0062	4
303	700	0.1593	0.0101	4
293	50	0.0437	0.0025	6
293	100	0.0651	0.0022	14
293	200	0.0811	0.0036	6
293	300	0.0901	0.0039	6
293	500	0.1269	0.0057	5
293	700	0.1448	0.0075	5
283	50	0.0658	0.0034	5
283	100	0.0642	0.0025	6
283	200	0.0870	0.0037	6
283	300	0.1082	0.0042	6
283	500	0.1336	0.0052	6
283	700	0.1507	0.0111	4
273	50	0.0607	0.0025	8
273	100	0.0751	0.0030	7
273	200	0.1066	0.0041	7
273	300	0.1163	0.0043	7

273	500	0.1363	0.0048	8
265	50	0.0677	0.0037	4
265	100	0.0846	0.0038	4
265	200	0.1069	0.0053	4
265	300	0.1211	0.0053	4
265	500	0.1616	0.0088	4
254	50	0.0735	0.0042	5
254	100	0.0744	0.0041	4
254	200	0.0929	0.0047	5
254	300	0.1212	0.0050	5
254	400	0.1461	0.0069	5

3.4.2 – Rate Constants for HOONO and $HONO_2$ Formation

Our measurements of α can be combined with measurements of the total rate constant k to determine individual rate constants for the formation of $HONO_2$ ($k_{3.1a}$) and HOONO ($k_{3.1b}$). Here, we use the $k_{3.1}$ measurements from the 2015 JPL data evaluation in order to determine these values. For termolecular reactions, we must fit data considering both the low-pressure and high-pressure limit, and thus the rate constants can be determined from

$$k(T) = \frac{k_0(T)M}{1+\frac{k_0(T)M}{k_\infty}} \times F_c^{\left(1+\log_{10}\left(\frac{k_0(T)M}{k_\infty(T)}\right)^2\right)^{-1}} \quad \text{(Equation 3.2)}$$

$$k_0(T) = k_0^{300}\left(\frac{T}{300}\right)^{-n} \quad \text{(Equation 3.3)}$$

$$k_\infty(T) = k_\infty^{300}\left(\frac{T}{300}\right)^{-m} \quad \text{(Equation 3.4)}$$

where k_0^{300} is the low-pressure limit rate constant at 300 K in $cm^6\ s^{-1}$, k_∞^{300} is the high-pressure limit rate constant at 300 K in $cm^3\ s^{-1}$, T is the temperature in K, M is the total density in cm^{-3}, and n and m are the temperature dependence of the low- and high-pressure rate constants, respectively, and are dimensionless. F_c describes the falloff region between the low- and high-pressure limits; here we use the JPL data evaluation recommendation of

F_c = 0.6, though it is worth noting that the IUPAC data evaluation recommends F_c = 0.41 for this reaction based on the calculations by Troe.[10]

The values obtained for $k_{3.1a}$ and $k_{3.1b}$ can be seen in Tables 3.2 and 3.3, respectively, as compared to the current recommendations from JPL and IUPAC. As can be seen in Figure 3.6, $k_{3.1b}$ is in the low-pressure limit for all experimental conditions studied here and therefore, the data is fit to

$$k(T) = k_0^{300}\left(\frac{T}{300}\right)^{-n} M \qquad \text{(Equation 3.5)}$$

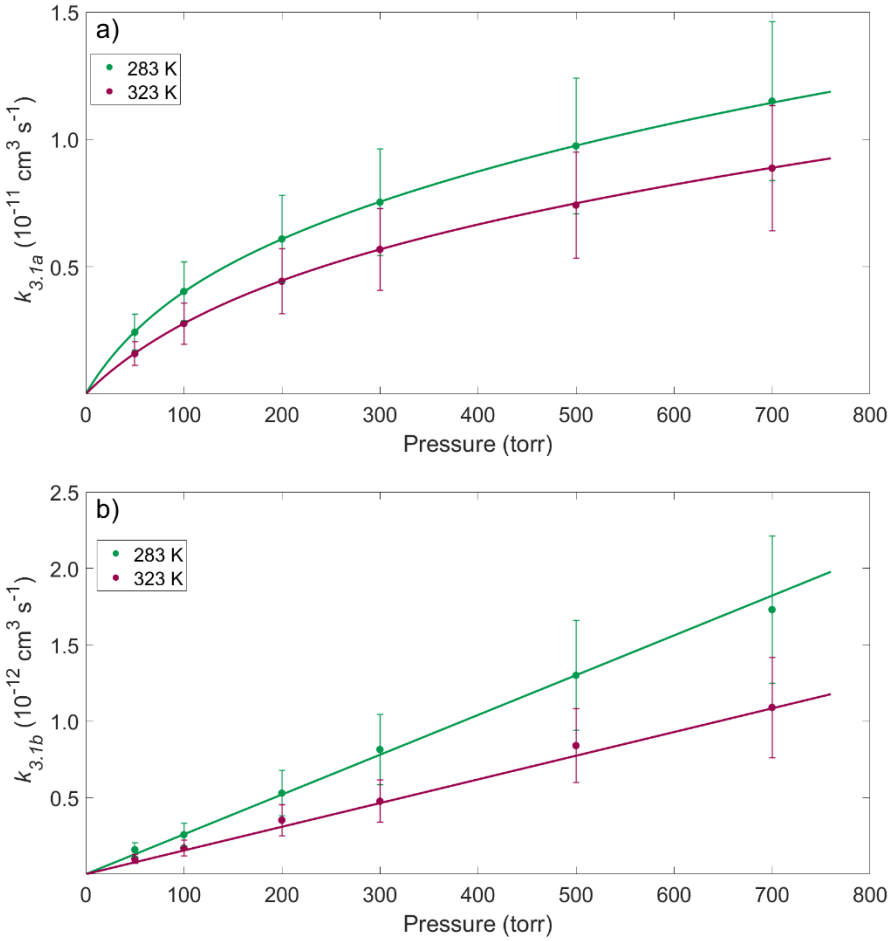

Figure 3.6: Rates of $k_{3.1a}$ (a) and $k_{3.1b}$ (b) at 283 and 323 K.

As Figure 3.7a and Table 3.2 demonstrate, the results from our determination of $k_{3.1a}$ is very close to the values from JPL. As we use the JPL value of $k_{3.1}$ and $F_c = 0.6$, this similarity is unsurprising. The IUPAC values for $k_{3.1a}$, on the other hand, are much larger than our value at low pressures, while there is still an offset at higher pressures. The difference between our $k_{3.1a}$ measurements and those from IUPAC are due to different values of $k_{3.1}$ between the JPL and IUPAC data evaluations. Resolution of this discrepancy in the total rate constant may bring all three of the measurements in line.

Table 3.2: Values of $k_{3.1a}$ determined in this work as compared to recommendations from the JPL and IUPAC data evaluations.

$k_{3.1a}$	k_0 (10^{-30} cm^6 s^{-1})	n	k_∞ (10^{-11} cm^3 s^{-1})	m	F_c
This work	1.80 ± 0.04	3.02 ± 0.023	2.90 ± 0.06	-0.04 ± 0.25	0.6[a]
JPL	1.8	3.0	2.8	0	0.6[a]
IUPAC	3.2	4.5	3.0	0	0.41

[a] Value fixed to 0.6

Table 3.3: Values of $k_{3.1b}$ determined in this work as compared to recommendations from the JPL and IUPAC data evaluations.

$k_{3.1b}$	k_0 (10^{-32} cm^6 s^{-1})	n	k_∞ (10^{-11} cm^3 s^{-1})	m	F_c
This work	6.43 ± 0.15	2.92 ± 0.25	-	-	0.6[a]
JPL	9.1	3.9	4.2	0.5	0.6[a]
IUPAC	10	4.5	3.5	0	0.41

[a] Value fixed to 0.6

Figure 3.7b shows that both the JPL and IUPAC values are much larger than our value of $k_{3.1b}$, as their k_0^{300} values are both almost 50% larger than our k_0^{300}. The IUPAC

values do approach our measurements at high pressures, however. Both the JPL and IUPAC data evaluations suggest that $k_{3.1b}$ is in the fall-off region under our experimental conditions, which is not consistent with our results. Further experiments extending our pressure and temperature range are clearly necessary in order to determine the high-pressure limit rate constants for $k_{3.1b}$.

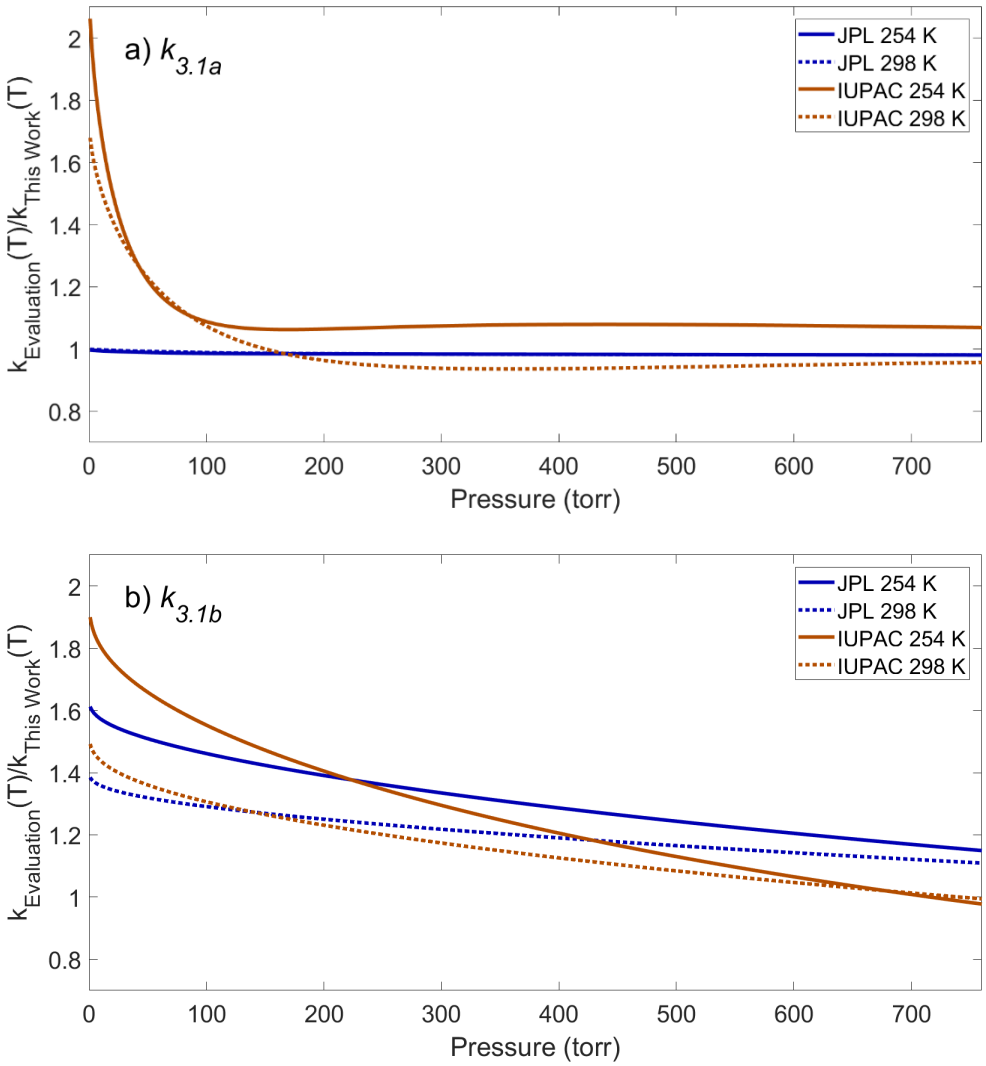

Figure 3.7: The ratio of the rate constants determined in this work for a) $k_{3.1a}$ and b) $k_{3.1b}$ to the values from the JPL and IUPAC data evaluations at 254 K and 298 K.

Despite the formation of HOONO representing a significant pathway for $k_{3.1}$ under atmospheric conditions, fate of HOONO is largely unknown. There are few experimental

or theoretical studies on its gas-phase photolysis or on reactions that lead to its destruction, with the exception of the calculations done by Fry et al.[7] They calculated the oscillator strengths of the $2\nu_1$ band of *cis-cis* HOONO in conjunction with the actinic flux at 1.4 μm and suggest its lifetime is less than 45 daylight hours. They also perform thermal decomposition calculations, which suggest that the lifetime of HOONO ranges from seconds at the surface to 38 days at the tropopause, making it the dominant loss mechanism in the lower troposphere. Current widely used models, such as GEOS-Chem[27] 12.6.1 (http://www.geos-chem.org/, accessed November 2019), do not include $k_{3.1b}$ at all, presumably assuming its lifetime is negligible before dissociating to OH + NO_2. Additional measurements of these loss mechanisms would further our knowledge of the fate of HOONO in the atmosphere.

3.5 – Conclusion

We have directly measured the branching ratio of the OH + NO_2 reaction as a function of both temperature and pressure over the ranges of 255 – 333 K and 50 – 700 torr using mid-infrared CRDS in the OH stretch region (3250 – 3630 cm^{-1}) and a newly developed temperature-controlled flow cell. By combining our data with previous measurements of the total rate constant, we have determined rate constants for both the HOONO and $HONO_2$ channels of this reaction. Comparison to the current JPL and IUPAC recommendations of these rate constants reveals disagreement between our $k_{3.1b}$ values, as they overestimate the production of HOONO, while our $k_{3.1a}$ measurements largely agree with the recommended values.

The reaction between OH and NO_2, despite its importance in urban environments and being the subject of numerous studies, remains a large source of uncertainty in current

atmospheric models. The inclusion of the data measured here into these recommendations may allow for refinement of these rates, particularly for $k_{3.1b}$. Further studies that extend the temperature and pressure range of these branching ratio measurements, and study the fate of HOONO in the atmosphere, are also necessary to better understand this reaction and its implications.

3.6 – References

1. Seinfeld, J. H.; Pandis, S. N., *Atmospheric Chemistry and Physics : From Air Pollution to Climate Change*, Third edition. ed.; John Wiley & Sons, Inc.: Hoboken, New Jersey, 2016, p xxvi, 1120 pages.

2. Martien, P. T.; Harley, R. A., Adjoint Sensitivity Analysis for a Three-Dimensional Photochemical Model: Application to Southern California. *Environ Sci Technol* **2006**, *40*, 4200-4210.

3. Robertshaw, J. S.; Smith, I. W. M., Kinetics of the OH + NO_2 + M Reaction at High Total Pressures. *J Phys Chem* **1982**, *86*, 785-790.

4. Nizkorodov, S. A.; Wennberg, P. O., First Spectroscopic Observation of Gas-Phase HOONO. *J Phys Chem A* **2002**, *106*, 855-859.

5. Drouin, B. J.; Fry, J. L.; Miller, C. E., Rotational Spectrum of *cis-cis* HOONO. *J Chem Phys* **2004**, *120*, 5505-5508.

6. Bean, B. D.; Mollner, A. K.; Nizkorodov, S. A.; Nair, G.; Okumura, M.; Sander, S. P.; Peterson, K. A.; Francisco, J. S., Cavity Ringdown Spectroscopy of *cis-cis* HOONO and the HOONO/$HONO_2$ Branching Ratio in the Reaction OH+NO_2+M. *J Phys Chem A* **2003**, *107*, 6974-6985.

7. Fry, J. L.; Nizkorodov, S. A.; Okumura, M.; Roehl, C. M.; Francisco, J. S.; Wennberg, P. O., *Cis-cis* and *trans-perp* HOONO: Action Spectroscopy and Isomerization Kinetics. *J Chem Phys* **2004**, *121*, 1432-1448.

8. Zhang, X.; Nimlos, M. R.; Ellison, G. B.; Varner, M. E.; Stanton, J. F., Infrared Absorption Spectra of Matrix-Isolated *cis-cis* HOONO and Its Ab Initio CCSD(T) Anharmonic Vibrational Bands. *J Chem Phys* **2006**, *124*.

9. Burkholder, J. B. S. S. P. A., J.; Barker, J. R.; Huie, R. E.; Kolb, C. E.; Kurylo, M. J.; Orkin, V. L.; Wilmouth, D. M.; Wine, P. H., Chemical Kinetics and Photochemical Data for Use in Atmospheric Studies, Evaluation No. 18. *JPL Publication 15-10, Jet Propulsion Laboratory, Pasadena, 2015* http://jpldataeval.jpl.nasa.gov **2015**.

10. Atkinson, R.; Baulch, D. L.; Cox, R. A.; Crowley, J. N.; Hampson, R. F.; Hynes, R. G.; Jenkin, M. E.; Rossi, M. J.; Troe, J., Evaluated Kinetic and Photochemical Data for Atmospheric Chemistry: Volume I - Gas Phase Reactions of O_x, HO_x, NO_x and SO_x Species. *Atmos Chem Phys* **2004**, *4*, 1461-1738.

11. Mollner, A. K.; Valluvadasan, S.; Feng, L.; Sprague, M. K.; Okumura, M.; Milligan, D. B.; Bloss, W. J.; Sander, S. P.; Martien, P. T.; Harley, R. A.; McCoy, A. B.; Carter, W. P. L.., Rate of Gas Phase Association of Hydroxyl Radical and Nitrogen Dioxide. *Science* **2010**, *330*, 646-649.

12. Hippler, H.; Krasteva, N.; Nasterlack, S.; Striebel, F., Reaction of OH+NO_2: High Pressure Experiments and Falloff Analysis. *J Phys Chem A* **2006**, *110*, 6781-6788.

13. Hippler, H.; Nasterlack, S.; Striebel, F., Reaction of OH+NO_2+M: Kinetic Evidence of Isomer Formation. *Phys Chem Chem Phys* **2002**, *4*, 2959-2964.

14. Troe, J., Refined Representation of Falloff Curves for the Reaction HO+NO_2+N_2 → ($HONO_2$, HOONO)+N_2. *J Phys Chem A* **2012**, *116*, 6387-6393.

15. B. Ruscic and D. H. Bross, *Active Thermochemical Tables (ATcT) values based on ver. 1.122g of the Thermochemical Network (2019); available at ATcT.anl.gov*.

16. Golden, D. M.; Barker, J. R.; Lohr, L. L., Master Equation Models for the Pressure- and Temperature-Dependant Reactions HO+NO_2 → $HONO_2$ and HO+NO_2 → HOONO. *J Phys Chem A* **2003**, *107*, 11057-11071.

17. Newsome, B.; Evans, M., Impact of Uncertainties in Inorganic Chemical Rate Constants on Tropospheric Composition and Ozone Radiative Forcing. *Atmos Chem Phys* **2017**, *17*, 14333-14352.

18. Sprague, M. K.; Garland, E. R.; Mollner, A. K.; Bloss, C.; Bean, B. D.; Weichman, M. L.; Mertens, L. A.; Okumura, M.; Sander, S. P., Kinetics of *n*-Butoxy and 2-Pentoxy Isomerization and Detection of Primary Products by Infrared Cavity Ringdown Spectroscopy. *J Phys Chem A* **2012**, *116*, 6327-6340.

19. Sprague, M. K.; Mertens, L. A.; Widgren, H. N.; Okumura, M.; Sander, S. P.; McCoy, A. B., Cavity Ringdown Spectroscopy of the Hydroxy-Methyl-Peroxy Radical. *J Phys Chem A* **2013**, *117*, 10006-10017.

20. Aker, P. M.; Sloan, J. J., The Initial Product Vibrational-Energy Distribution in the Reaction between O($^1D_2$) and H_2. *J Chem Phys* **1986**, *85*, 1412-1417.

21. Cheskis, S. G.; Iogansen, A. A.; Kulakov, P. V.; Razuvaev, I. Y.; Sarkisov, O. M.; Titov, A. A., OH Vibrational Distribution in the Reaction O(^1D)+CH_4. *Chem Phys Lett* **1989**, *155*, 37-42.

22. Smith, I. W. M.; Williams, M. D., Vibrational Relaxation of OH (v=1) and OD (v=1) by HNO_3, DNO_3, H_2O, NO and NO_2. *J Chem Soc Farad T 2* **1985**, *81*, 1849-1860.

23. Sharpe, S. W.; Johnson, T. J.; Sams, R. L.; Chu, P. M.; Rhoderick, G. C.; Johnson, P. A., Gas-Phase Databases for Quantitative Infrared Spectroscopy. *Appl Spectrosc* **2004**, *58*, 1452-1461.

24. McCoy, A. B.; Sprague, M. K.; Okumura, M., The Role of Torsion/Torsion Coupling in the Vibrational Spectrum of *cis-cis* HOONO. *J Phys Chem A* **2010**, *114*, 1324-1333.

25. Chackerian, C.; Sharpe, S. W.; Blake, T. A., Anhydrous Nitric Acid Integrated Absorption Cross Sections: 820-5300 cm^{-1}. *J Quant Spectrosc Ra* **2003**, *82*, 429-441.

26. Yalin, A. P.; Zare, R. N., Effect of Laser Lineshape on the Quantitative Analysis of Cavity Ring-Down Signals. *Laser Phys* **2002**, *12*, 1065-1072.

27. Bey, I.; Jacob, D. J.; Yantosca, R. M.; Logan, J. A.; Field, B. D.; Fiore, A. M.; Li, Q. B.; Liu, H. G. Y.; Mickley, L. J.; Schultz, M. G., Global Modeling of Tropospheric Chemistry with Assimilated Meteorology: Model Description and Evaluation. *J Geophys Res-Atmos* **2001**, *106*, 23073-23095.